Enceladus's South Polar Sea

Geoffrey C. Collins [a,*] and Jason C. Goodman [b]

[a] Physics and Astronomy Department, Wheaton College, Norton MA 02766, USA.

[*] Corresponding Author email address: gcollins@wheatonma.edu

[b] Physical Oceanography Department, Woods Hole Oceanographic Institution,

Woods Hole MA 02543, USA.

Submitted to *Icarus*, November 3, 2006

Revised January 23, 2007

ABSTRACT
Recent observations of the south pole of Saturn's moon Enceladus by the Cassini spacecraft have revealed an active world, powered by internal heat. In this paper, we propose that localized subsurface melting on Enceladus has produced an internal south polar sea. Evidence for this localized sea comes from the shape of Enceladus, which does not match a differentiated body at its current orbital position. We show that melting induced by the observed heat flow at the south pole produces a large enough pit to match the shape of Enceladus with a differentiated rock and ice interior. Numerical modeling of melting and ice flow shows that the sea produced beneath the south pole is stable against inflow of ductile ice from its surroundings for the duration of the heating. The shape modification due to melting also produces a negative degree-two gravity anomaly, which can reorient the spin axis of Enceladus in order to place the sea at the pole.

Key Words: Enceladus; Satellites, Shapes; Interiors; Geophysics

1. Introduction

The south polar region of Saturn's satellite Enceladus has attracted recent attention due to its large, internally generated thermal anomaly (Spencer *et al*., 2006), plumes of water and other material jetting from cracks in the surface (Porco *et al*., 2006; Hansen *et al*., 2006; Spahn *et al*., 2006; Waite *et al*., 2006), and the young fractured terrain surrounding the pole (Porco *et al*., 2006). These observations imply a thin ice lithosphere and possibly a source of liquid near the surface. This view is at odds with the interpretation by Porco *et al*. (2006) that the shape of Enceladus most closely matches an undifferentiated body, which would require a cold, stiff interior throughout solar system history, or that it supports significant non-hydrostatic topography if it is differentiated. In this paper, we propose an alternative explanation for the shape of Enceladus, in which localized heating and subsequent melting at the base of the ice shell on Enceladus has produced an internal south polar sea. Our goal in building this explanation is to simultaneously take into account the observed shape of Enceladus, its likely differentiated interior structure, the heat flow and sharp change in geological activity observed in the south polar terrain, and the location of the anomalous region at the pole.

2. Heat flow in Encealdus

In this section, we examine the response of the ice shell of Enceladus to the application of basal heat, to test if subsurface melting is the likely response. If the interior of Enceladus was warmed only by internal radiogenic heat sources, its power output would be about 300 MW (Kargel, 2006). A conductive heat balance shows that this is insufficient to cause basal melting, even in a thick ice shell, without calling for unusual ices or insulating layers. For reasonable water ice shell thicknesses (50 to 100 km) in the radiogenic-only scenario, basal temperatures only reach 10 - 30 K above the surface temperature. The south polar terrain has been measured to be currently radiating 3 - 7 GW of power (Spencer *et al*., 2006), over ten times the expected radiogenic output. Tidal heating driven by an eccentric orbit pumped by a near-resonance with Dione is the probable source of the extra interior energy (Squyres *et al*., 1983). The tidal dissipation may be taking place in the ice shell, the rocky core, or a combination of the two. If

dissipation began in the rocky core while the outer ice layer of Enceladus was in the deeply frozen radiogenic-only state, the interior heating would begin to warm and possibly melt the overlying ice. The presence of propane and acetylene in the south polar geysers strongly suggests that the water on Enceladus is in contact with a hot silicate interior (Matson *et al*., 2006). Regardless of the exact source of the heat, localized heating at the base of the ice shell must be transferred out through conduction, convection, or melting.

Which one of these heat transfer processes is dominant depends on the thickness of the shell and the rate at which heat must be transferred out of the shell. To a first order, we can compare the typical timescale of conduction through the ice shell, $\tau_{cond} = D^2 \kappa^{-1}$ (where the thermal diffusivity $\kappa = 10^{-6}$ m^2 s^{-1} for ice) to the time it would take a certain power output to warm and melt an ice shell of the same thickness,

$$\tau_{melt} = (L + C_p \Delta T) D \rho_{ice} / F_{base} \quad (1)$$

where L is the latent heat of fusion, C_p is the heat capacity, ΔT is the temperature rise (~200 K) to the melting point, ρ_{ice} is the ice density, and F_{base} is the basal heat flow. Comparing the melting and conduction timescales, it should be noted that τ_{cond} scales with D^2, while τ_{melt} scales linearly with D, so beyond some thickness it is faster to melt the ice than to conduct the heat out. Another factor favoring melting at the base of the ice shell is that the area over which the heat is distributed shrinks with increasing depth due to the spherical geometry, speeding τ_{melt} at depth. Figure 1 shows the ratio $\tau_{cond} / \tau_{melt}$ calculated with ice parameter values from Table A1, and the range of observed power output in the south polar terrain. Power output is converted to heat flux by dividing by the depth-averaged area of the ice shell poleward of 50°S. For $D > 20$ km, τ_{melt} is shorter than τ_{cond} and melting will dominate over conduction. Eventually, as the ice shell thins due to melting, conduction will balance further melting. The equilibrium thickness of a column of ice heated from below can be described by a simple one-dimensional insulation equation:

$$h = F_{\mathrm{base}}^{-1} \int_{T_s}^{T_m} k dT \quad (2)$$

where F_{base} is the basal heat flux, T_s and T_m are the temperatures at the surface and base of the ice sheet, and k is the (temperature-dependent) thermal conductivity of ice.

[Figure 1]

What about the role of convection? The initiation of convection has been studied for the Galilean satellites using the appropriate composite rheology for water ice (Barr and Pappalardo, 2005), and is found to be strongly dependent on grain size. Convection initiation on Europa has been well-studied, and Barr and Pappalardo have found that thicker ice shells are generally required to initiate convection than what would be expected from a simple Newtonian rheology. Compared to Europa, gravity on Enceladus is more than a factor of 10 lower (0.11 m s^{-2}), which decreases the buoyancy stress driving convection; and the surface temperature is ~25 K lower, which increases the Rayleigh number, but also increases the thickness of the stagnant lid. Barr and McKinnon (*Geophys. Res. Lett.*, submitted) have extended the work on convection initiation to Enceladus, and find that the ice shell is remarkably stable against convection, with the critical Rayleigh number only being met for an ice shell ~ 100 km thick with a 1 mm grain size, and for thinner ice shells if the grain size is smaller.

We can use the preceding discussion of conduction versus melting to also assess the role of convection versus melting. The Nusselt number *Nu* normalizes the heat flow due to convection to the heat flow due to conduction. *Nu* is near unity near the critical Rayleigh number, and increases with increasing shell thickness. We calculate *Nu* for stagnant lid ice convection using the fitting parameters of Solomatov (1995) and volume diffusion with grain size ~ 0.1 mm (Barr and McKinnon, *Geophys. Res. Lett.*, submitted), and plot this curve on Figure 1. Since the critical Rayleigh number is not reached until the ice is more than twice as thick as the τ_{cond} / τ_{melt} crossover point, and *Nu* scales almost linearly with *D* (Solomatov, 1995), convection will not be able to carry away heat faster than the ice will melt. As melting proceeds, the shell will thin, lowering the Rayleigh number and eventually shutting off the possibility of convection entirely. The only way for convection to beat melting in this first-order analysis is to lower the heat flow below the observed power output from the south pole.

3. Modeling the Formation of a Localized Sea

We now turn to modeling the ice shell melting process in detail. In our model, Enceladus begins with a conductive ice layer, warmed only by radiogenic heating from the rocky interior. Then tidal heating initiates, producing a hot spot at the base of the ice shell, which in turn warms and melts the overlying ice. The surface first bows up slightly as the ice thermally expands, but this is quickly overwhelmed by vertical contraction of the ice shell due to subsurface melting. As the local pool of melt grows, isostatic compensation creates a large pit on the surface, and the surrounding subsurface ice begins to flow toward the melt pool. The melt pool will grow until the volume of ice lost through melting is balanced both by the inflow of surrounding ice and by increased energy radiated into space as the surface ice warms. We deliberately use the term "sea" to describe this localized melt pool, as opposed to "ocean" which has come to imply a global layer of liquid water in the icy satellite literature.

To investigate this scenario in detail, we used a finite difference model for thermal conduction and ice flow in an axisymmetric 2D cylindrical coordinate system. The model begins as a flat ice sheet in thermal conductive equilibrium with interior radiogenic heating, and at time 0 we apply 3 or 7 GW of heat in a Gaussian bump profile 300 km in diameter to the base of the ice. The grid is regularly spaced with distance from the center, and the vertical grid spacing has a fixed number of levels evenly spaced from bottom to top, so vertical resolution increases as the ice shell thins. The model solves 2D thermal conduction equations on this grid, and the surface blackbody energy balance determines the surface temperature. A full description of the model physics is contained in Appendix A. The bottom of the model starts frozen, due to the initial radiogenic-only condition, and the energy balance at the base of the ice determines the melting or freezing rate. Ice flow is included, using the stress-strain relationship of Goldsby and Kohlstedt (2001), assuming a 1-mm grain size, and ice flow transports both mass and temperature in the model. The upper surface is assumed to be rigid, and isostatic adjustment of the ice shell includes both Airy (shell thickness) and Pratt (thermal buoyancy) compensation. Our model dynamics allow horizontal ice flow to advect heat, but do not permit whole-shell convective diapirism. This is justified by our discussion in Section 2 above.

[Figure 2]

Two endmember model runs for Enceladus are shown in Figure 2. The fast

melting model shows a 7 GW heat source applied to the base of a 39 km thick ice shell, while the slow melting model shows a 3 GW heat source applied to the base of a 61 km thick ice shell. The fast melting model reaches an equilibrium ice thickness of 3.9 km at the center in 4 million years, while the slow melting model reaches an equilibrium ice thickness of 9.6 km in 15 million years. Isostatic compensation creates surface depressions 3.3-2.3 km deep in the two models. Ice inflow from the sides is significant, but the weak gravity and cold temperatures from the radiogenic-only starting conditions make this ice flow relatively sluggish compared to similar models for Europa (Stevenson, 2000; O'Brien *et al*., 2002; Goodman and Collins, manuscript in preparation). Flow is negligible for ice colder than 200K (dashed line in Figure 2), and the final profile is not strongly grain-size-dependent. Despite the complexity of our numerical model, we find that the equilibrium remnant ice thickness at r=0 is in agreement with equation 2, above.

To test the stability of this sea over time, Figure 3 shows a continuation of the simulation beyond the 20 million years shown in Figure 2. We find that as the sea approaches its equilibrium shape, ice flow broadens the hole by no more than 10% over 50 million years. This broadening is the result of ice from the outside base of the sea flowing up the sloped ice/water interface, and then melting when it reaches an area of higher heat flow. Melting of inflowing ice near the top of the ice/water interface is balanced by freezing of new ice to the base of the ice/water interface at the outer margins. The approach to the equilibrium shape is asymptotic in the numerical model, which gives us confidence that this shape is stable against inflow of ice as long as the heat source persists.

[Figure 3]

Ductile flow at the base of the ice layer is the crucial factor that determines if the melt will be stable as an isolated sea, or if it will spread out into a global ocean. Unless ductile flow of ice over the sea transports mass radially inward, there is no pressure gradient at the to drive liquid intrusion beneath the ice at the boundary where the ice, water, and rock meet. In any case, such an intrusion under the ice would freeze rapidly unless the basal ice is already near the melting point. The cold radiogenic-only basal conditions for the ice shell on Enceladus will only allow significant ice flow where there is anomalous heating, so creating a global ocean on Enceladus would require basal heating to nearly the point of melting over the whole globe. If instead most of the anomalous heating is concentrated in one location for a significant period of time (as the observations suggest), then we should expect an isolated sea to form in response.

4. Melting and the Shape of Enceladus

The large radius and depth of the pit created by melting the localized sea will have a significant effect on the observed shape of Enceladus. Porco *et al.* (2006) reported that the shape of Enceladus is best fit by an ellipsoid with a tidal axis a of 256.6±0.5 km, an intermediate equatorial axis b of 251.4±0.2 km, and a polar axis c of 248.3±0.2 km. Recasting these observations as pairs of axes, the observed value of b - c is about 3 km and a - c is about 8 km. Note that the larger error bars on the a axis allow more flexibility in the observed value of a - c. If Enceladus is taken to be in hydrostatic equilibrium with an effective radius of 252.1±0.2 km, then Porco *et al*. (2006) argue that its shape may be best explained by a homogeneous body of mixed rock and ice. At its current orbital position, a homogeneous Enceladus in hydrostatic equilibrium would have

a *b* axis of 250.8 km, 0.4 km smaller than the lower limit of the observational error, and a *c* axis of 248.8 km, 0.3 km larger than the upper limit of the observational error. In other words, *b* - *c* for a homogeneous Enceladus in equilibrium is about a kilometer smaller than what is observed. Increasing the differentiation of Enceladus would decrease the amplitude of the tidal and rotational distortions as more mass is concentrated into the interior (Dermott, 1979), so a differentiated body is more spherical. This would lengthen the *b* axis by a small amount, while the *a* axis would be significantly shortened and the *c* axis would be significantly lengthened. This would have the effect of making both the *a* - *c* and the *b* - *c* values much smaller than observed, which is why Porco *et al.* advocated the homogeneous model (or alternatively, that Enceladus supports significant non-hydrostatic loads). However, if the length of the *c* axis could be modified independently of the other axes, an accurate fit to observations might be obtained.

Porco *et al.* also observed that the greatest longitudinally-averaged deviations from the best-fit ellipsoid are found at the south pole, which is 0.4 km below the ellipsoid, and at 50°S, which rises 0.4 km above the ellipsoid (Porco *et al*., 2006). The observed deviations from the best-fit ellipsoid at these two locations are consistent with a cap, centered on the south pole, with a greater radius of curvature than the best-fit ellipsoid. In other words, the ellipsoid is flattening out at the south pole. We interpret this as evidence of the south polar surface sinking as a result of the formation of a south polar sea (Figure 4), and we show below that the observed shape of Enceladus can be more precisely matched when the effect of melting is taken into account.

[Figure 4]

If we think about the problem in simple terms, the formation of a south polar sea of thickness d_{sea} would shorten the radius of the satellite at the south pole by d_{sea} (ρ_{water} - ρ_{ice}) / ρ_{water}. Since the northern hemisphere is not affected by this melting, the overall *c* axis length will shorten by half this amount. Shortening the *c* axis through melting without affecting the *a* and *b* axes would allow us to construct equilibrium ellipsoids of Enceladus with differentiated interiors that meet the observed *a* - *c* and *b* - *c* values. For example, a differentiated Enceladus in hydrostatic equilibrium, with a core of density 2600 kg m^{-3} would have an *a* - *c* of 5.9 km and a *b* - *c* of 1.5 km, and an ice shell 66 km thick. Creating a pit 3.4 km deep by melting ~70% of the ice shell at the south pole would change *a* - *c* to 7.6 km and *b* - *c* to 3.2 km, both within the observed range.

However, the simple analysis above has a serious shortcoming. While a melt-generated pit at the south pole could lower the pole-to-pole diameter of Enceladus by a few kilometers, it does not necessarily explain the entire shape of Enceladus. Suppose, for example, that a melting event somehow generated a south polar pit 3.4 km deep, but only 5 km wide. Such a pit would correctly depress the elevation of the south pole, but elsewhere the shape would not look much like observations. Indeed, we can take the hydrostatic ellipsoid from the simple example above, subtract from it a 3.4 km surface depression centered on the south pole, with the width and shape predicted by our numerical model of shell melting in section 3 above, and then compute a new best-fit ellipsoid to the modified shape (Figure 5). Though the lengths of the body in the *a*, *b*, and *c* axis directions are correct as in the simple example above, the axes of the best-fit ellipsoid to the overall shape do not match the values observed by Porco *et al*. (2006). In particular, the *c* axis of the best-fit ellipsoid is significantly larger than the observed axis. Deviations of the calculated surface from the best-fit ellipsoid are in the correct locations,

low at the south pole and high at 50°S latitude, but their magnitudes are 1.5 km, almost three times the residual topography reported by Porco *et al*. at these locations. Interestingly, the smaller regional low at 15°N and regional high at the north pole also appear to be features of the observed shape data from Enceladus (Thomas *et al*., *Icarus*, submitted). From the shortcomings of this simple forward approach to the problem, an inverse approach to the problem suggests itself, as described in the next section.

[Figure 5]

5. Inverse Calculation of Required Heating from the Shape of Enceladus

While the ice shell melting model discussed previously shows that our hypothesis has merit, it does not exactly reproduce the observed shape of Enceladus. However, the Gaussian-bump shaped melting profile used in our numerical model is an arbitrary choice, since we have no information on the actual distribution of heat at the base of the ice. Apart from an estimated 3 - 7 GW of heat emitted from the surface of the south polar terrain (Spencer *et al*., 2006), the shape and size of the basal heating is entirely unconstrained.

However, the shape of Enceladus is fairly well constrained, which suggests that an inverse approach to the problem will be more profitable. If we compute the difference between a proposed initial hydrostatically-equilibrated ellipsoid shape and the measured modern shape of Enceladus, our hypothesis will succeed if we find some reasonable heating profile which would melt the initial ellipsoid to produce the modern shape. In particular, we require the following to be true:

A) The heat source is radially symmetric about the south pole. This is the simplest hypothesis in the absence of other information about the heat source.
B) The axial lengths of the modified ellipsoid should be consistent with the best-fit ellipsoid observed by Porco *et al*. (2006).
C) The initial and modified ellipsoids must be nearly identical in the northern hemisphere, since we propose a melt event focused on the south pole.
D) Since subsurface melting can only cause pits, the modified shape must not have higher topography than our proposed initial ellipsoid.
E) Where the modified ellipsoid is lower than the initial ellipsoid, the pit depth must not exceed what could be produced by volume contraction upon melting the entire ice layer.
F) The overall heat flux needed to thin the ice and explain the modern shape of Enceladus must be consistent with the observed excess heat output of 3-7 GW.

It would be difficult to compute the heat flux required to produce a given pit shape were the full physics of our melting and ice flow model included, since it would require us to construct a full adjoint version of the model. However, our results from Section 3 show that most of the detailed model physics is not important for explaining the final shape of the surface topography: the role of ice flow is minor, lateral heat conduction plays a small role, and a simple vertical heat conduction equation explains the final thickness quite well.

We use the following procedure to attempt to find a basal heating and melting profile which would explain the current shape of Enceladus:

1) Construct a shape model (radius as a function of latitude, in the a - c and b - c axis planes) for Enceladus based on the observations reported by Porco *et al*. (2006). We use an ellipsoid with axes $a_0 = 256.6$, $b_0 = 251.4$, $c_0 = 248.3$, and then add to it a perturbation based on the residuals described by Porco *et al*.: 400 m below the ellipsoid at the south pole, 400 m above the ellipsoid at 50°S. Since we do not have the original data observed by Porco *et al*., we approximate this perturbation with the expression: $-0.4 \cos(-4.5\ \theta) \exp(\theta^8)$ where θ is the angular distance from the south pole (in radians). The exact choice of expression does not make a large difference to the results, as long as the residual topography has this general shape. Initial comparison of the curve generated by this expression to the residual topography reported by Thomas *et al*. (*Icarus*, submitted) shows a close match to the shape of the south polar pit and its surroundings.
2) Construct a shape model for our proposed original, unmelted Enceladus. For a given core density ρ_0 and initial mean radius r_0, we compute the hydrostatic equilibrium shape and axes (a, b, c) using the method of Dermott (1979).
3) The vertical offset z_0 between these two shapes along the north-south axis is a free parameter. This offset must be adjusted so that the unmelted shape model is as coincident as possible in the northern hemisphere with the observed best-fit ellipsoid. We find the best fit in the northern hemisphere for $z_0 = 0.825\ (c_0 - c)$. Everywhere else, the difference Δr between the two shapes is, we assume, due to melting of the ice shell.
4) Compute the implied thickness h of remnant ice which would produce a surface depression of depth Δr in a shell with an initial thickness D, using the equation
$$(D - h)\ (\rho_{water} - \rho_{ice}) / \rho_{water} = \Delta r \qquad (3)$$
5) Using Eq. (2), find the basal heat flux as a function of latitude necessary to melt the ice shell to a thickness h.
6) Integrate this basal heat flux over the entire southern hemisphere to find the total power output.
7) Check to ensure that the shape differences Δr, the implied thickness h, and the implied power output are consistent with requirements A-F above.

[Figure 6]

The result of one such inverse calculation is shown in Figure 6. In this example, we assume a core density of 2600 kg m^{-3} and a mean radius before melting of 252.6 km. The hydrostatic ellipsoid consistent with these assumptions is indicated by the thin lines in the top panel. Remember, this profile has been shifted northward by z_0. To explain the difference between this shape and the figure reported by Porco *et al*., we require a surface depression shaped as in the second panel. Using Eq. 2, we find that a total heat output of 7 GW, distributed as shown in the bottom panel, would produce a surface depression that matches the observed shape of Enceladus. Note that the required sea is broader than that produced by the Gaussian bump heat source in section 3. There are three possibilities to explain this: (a) the arbitrary Gaussian heat distribution we assumed was the wrong heating profile to use; (b) lateral transport of warm water in the sea is spreading the basal heat source over a larger area of ice; and (c) flow of warm ice from the edge toward the center of the sea has spread out the profile of the pit, as shown in Figure 3. All of these possibilities are likely, and have probably worked together to spread out the profile of the pit.

[Figure 7]

We have repeated this analysis for a wide range of core densities and initial mean radii, and summarize the results on Figure 7. In the dark grey zone on the left side of each panel of Figure 7 (at smaller core densities), our shape model violates requirement E: the surface ice layer is too thin to allow a large enough south polar depression to be created by melting, even if the entire ice layer is melted. The light grey zones indicate parameter choices which require a heat source greater than 7 GW (left side) or less than 3 GW (right side). The thin contours on Figure 7 indicate the degree to which requirement C is satisfied: they indicate the worst mismatch between our proposed shape and the Porco *et al*. ellipsoid in the A-C and B-C planes.

[Figure 8]

In Figure 8, we test requirement B, plotting the difference between the *a* and *b* axes of our proposed original ellipsoids and the value reported by Porco *et al*. We find a substantial area of parameter space where our ellipsoids agree within the error range reported by Porco *et al*. (±500 m in *a*, ±200 m in *b*). The *c* axes automatically agree by the construction of our inverse problem. While many of our proposed original ellipsoids have mean radii greater than the reported value of 252.1 km, formation of the polar depression reduces the mean radius of the best-fit ellipsoid to the observations. By the construction of the inverse problem, the final melted shapes all have mean radii that match the observed value.

Our best estimate, based on the inverse model, is that Enceladus has a core density of 2600 kg m^{-3} and started with a mean radius of 252.6 km (the point marked with an X on Figures 7 and 8). As shown by the contours on Figures 7 and 8, the area surrounding this point is the best compromise between misfits in the A-C and B-C planes, the length of the *a* and *b* axes, and the 7 GW power output limit. Better estimates for the observed *a* axis radius will help to narrow the possible core densities and starting radii.

Our proposed shape contains residual features not reported by Porco *et al*. Because the northern hemisphere is unmodified from the original ellipsoid and simply shifted northward, it is a few hundred meters too low at a latitude of about 20° N, and a few hundred meters too high at the north pole (this is where most of the misfit plotted in figure 7 arises). The deviations are largest in the A-C plane, which appears to be the least constrained part of the observed shape of Enceladus, since Porco *et al*. assign it the largest error bars. Comparison of these misfits with the observed deviations of Enceladus's true figure from the best-fit ellipsoid will help to confirm if Enceladus started with a different equilibrium figure that has since been modified by melting.

6. Melting and Reorientation

Why are the thermal anomaly and the geysers on Enceladus centered at the south pole? Nimmo and Pappalardo (2006) describe a scenario for reorienting the spin axis of Enceladus in which stacked diapirs of hot, low-density rock and warm, low-density ice in the interior of Enceladus will produce a torque that drives the low density diapirs toward the pole. To produce this torque, the diapirs must produce a negative degree-two gravity anomaly. To produce this anomaly, they must be largely isostatically uncompensated, implying that the surface ice must be rigid.

The same polar wander mechanism described by Nimmo and Pappalardo will also operate for a pool of melt which is denser than the surrounding ice, as long as it is

isostatically compensated, creating a large surface pit. Using the method discussed by Nimmo and Pappalardo, we can numerically determine the degree-two component of the gravity anomaly (Δg_{20}) associated with the surface pit and underlying sea. Nimmo and Pappalardo's approach is applicable to a cylindrical density anomaly, so we approximate the more complicated shape of our "sea" as the sum of a set of thin stacked cylinders. Using the shape of the sea shown in Figure 9, we estimate a Δg_{20} perturbation of -2.6 mgal at 100 km altitude. Nimmo and Pappalardo's ice diapir model can produce larger gravity anomalies than this, but only by using density anomalies of 100 kg/m^3, an unrealistically high value for thermal diapirism and requiring compositional differences within the ice shell instead.

[Figure 9]

Thus if the thermal anomaly originally started in the southern midlatitudes instead of at the south pole, the gravity anomaly associated with the production of a localized sea and surface depression can reorient Enceladus by a modest amount, moving the sea toward the pole. We believe that an isostatically compensated sea is more consistent with the observations of south polar geology, heat flow, and global shape than the thick, stiff lithosphere required by the ice diapir model and the slight doming of the *c* axis it produces. As we argued in section 2, it may be difficult to form a thermal diapir on Enceladus instead of melting the ice, given the observed south polar heat flow. Since the melting of the sea would be driven by a thermal anomaly in the silicate core, reorientation due to a hot, low density diapir in the rocky core coupled with a compensated melt pool within the ice shell could provide a strong, self-consistent mechanism for the reorientation of Enceladus.

7. Conclusion

We have proposed a hypothesis for a south polar sea on Enceladus that simultaneously reconciles the shape of a differentiated Enceladus with the observed shape, explains the concentration of geologic activity and heat flow by melting, and supports the south polar location by reorientation of the spin axis. The observed thermal energy radiating from the south pole is the correct amount of power necessary to produce and maintain a surface pit that will transform an equilibrium differentiated ellipsoid into the currently observed shape of Enceladus. Our best fits of melt-modified differentiated equilibrium ellipsoids to the reported shape of Enceladus predict that the core density is close to 2600 kg m^{-3}. In short, the combination of a warm, currently active south pole with the observed shape of Enceladus is a big clue pointing to the possible existence of a south polar sea below the ice.

Detailed analysis of the complex tectonics surrounding the south pole of Enceladus will help to test the south polar sea hypothesis, and initial observations show symmetrical patterns of tectonic features centered on the south pole (Porco *et al*., 2006). Possible contractional features reported parallel to the south polar terrain boundary are consistent with radial contraction of the south polar terrain as it subsides over a melting sea, since the production of a 3 km deep surface pit will shorten lines of longitude by about 1% in the south polar terrain. Reconstruction of detailed topography of the south polar area will help to distinguish how much of the shape anomaly is due to short-wavelength tectonic structures, and how much of it may be attributable to a south polar sea.

Another necessary constraint is the total amount of mass that has been lost from Enceladus due to geyser activity, since this may act in concert with melting to produce a south polar pit. If the geysers tap into the sea itself, our assumption of a conductive lid over the sea would need to be reexamined, since advection of heat by water moving up through cracks could be a significant heat loss mechanism.

Future attempts by Cassini to determine the gravity field of Enceladus are crucial to testing this hypothesis. Determination of the axial moment of inertia, and thus the interior differentiation state, can test our prediction of the rocky core density of Enceladus. Determination of south polar topography and the existence and shape of a gravity anomaly over the south pole is especially important, as it will be able to test the reorientation hypothesis and possibly distinguish between the diapiric and melting models for the origin of the anomaly.

Acknowledgements

We would like to thank Amy Barr, Francis Nimmo, Bob Pappalardo, and John Spencer for productive discussions which stimulated ideas for this paper. Peter Thomas and an anonymous reviewer helped greatly to reshape and refine this paper.

References

Barr, A.C., Pappalardo, R.T., 2005. Onset of convection in the icy Galilean satellites: Influence of rheology. J. Geophys. Res., 110, E12005.

Dermott, S.F., 1979. Shapes and gravitational moments of satellites and asteroids. Icarus 37, 575-586.

Dorsey, N. E., 1940. Properties of Ordinary Water-Substance in all its Phases: Water-Vapor, Water, and all the Ices. Reinhold, New York.

Eisenberg, D., Kauzmann, W., 1969. The Structure and Properties of Water. Oxford University Press, Oxford.

Goldsby, D.L., Kohlstedt, D.L., 2001. Superplastic deformation of ice: Experimental observations. J. Geophys. Res., 106, 11,017-11,030.

Hansen, C.J., Esposito, L., Stewart, A.I.F., Colwell, J., Hendrix, A., Pryor, W., Shemansky, D., West, R., 2006. Enceladus' water vapor plume. Science 311, 1422-1425.

Hobbs, P.V., 1974. Ice Physics. Clarendon Press, Oxford.

Kargel, J.S., 2006. Enceladus: Cosmic gymnast, volatile miniworld. Science 311, 1389-1391.

Matson, D.L., Castillo, J.C., Lunine, J., Johnson, T.V., 2006. Enceladus' plume: Compositional evidence for a hot interior. Icarus, doi:10.1016/j.icarus.2006.10.016.

Nimmo, F., Pappalardo, R.T., 2006. Diapir-induced reorientation of Saturn's moon Enceladus. Nature 441, 614-616.

O'Brien, D.P., Geissler, P., Greenberg, R., 2002. A melt-through model for chaos formation on Europa. Icarus 156, 152-161.

Porco, C.C., and 24 colleagues, 2006. Cassini observes the active south pole of Enceladus. Science 311, 1393-1401.

Solomatov, V.S., 1995. Scaling of temperature- and stress-dependent viscosity convection. Phys. Fluids 7, 266-274.

Spahn, F., and 15 colleagues, 2006. Cassini dust measurements at Enceladus and implications for the origin of the E ring. Science 311, 1416-1418.

Spencer, J.R., Pearl, J.C., Segura, M., Flasar, F.M., Mamoutkine, A., Romani, P., Buratti, B.J., Hendrix, A.R., Spilker, L.J., Lopes, R.M.C., 2006. Cassini encounters Enceladus: Background and the discovery of a south polar hot spot. Science 311, 1401-1405.

Squyres, S.W., Reynolds, R.T., Cassen, P.M., Peale, S.J., 1983. The evolution of Enceladus, Icarus 53, 319-331.

Stevenson, D.J., 2000. Limits on the variation of thickness of Europa's ice shell. Lunar Planet. Sci. XXXI, 1506 (abstract).

Waite, J.H., and 13 colleagues, 2006. Cassini ion and neutral mass spectrometer: Enceladus plume composition and structure. Science 311, 1419-1422.

Appendix A: Two-dimensional Ice Shell Melting Model, with Viscous Flow

Here, we describe the key parameters of the ice shell melting model used in section 3 of this study.

Physical System: The model solves the thermal advection/conduction equation for ice in cylindrical coordinates:

$$\rho_i C_p \left(\frac{\partial}{\partial t} T + u \frac{\partial}{\partial r} T \right) = \frac{1}{r} \frac{\partial}{\partial r} \left(r k \frac{\partial}{\partial r} T \right) + \frac{\partial}{\partial z} \left(k \frac{\partial}{\partial z} T \right) \tag{A1}$$

where T is temperature, u is radial flow velocity, k is thermal conductivity, ρ_i is ice density (the ice is assumed to be pure H_2O), and C_p is heat capacity. The latter three quantities are all functions of temperature (see Table A1). The z coordinate is set to zero at some arbitrary equipotential (we choose the "sea level" surface which would result if all ice were melted), and we use the terms z_0 and z_b to denote the locations of the upper and lower ice surfaces, respectively.

[Table A1]

At the lower boundary, energy balance requires:

$$L \rho_i M = k \frac{\partial}{\partial z} T + F_{\text{base}} \tag{A2}$$

where L is the latent heat of fusion of water, M is the basal melting rate in m s^{-1}, and F_{base} is the heat flux applied to the base. When the ice base is grounded against bedrock, we require $M = 0$ *unless* this would imply a basal temperature $T(z_b) > T_f$ (the freezing point, assumed to be 273 K for our experiments). If so, the ice base must be in contact with liquid, in which case we require $T(z_b) = T_f$.

At the upper boundary, energy balance requires:

$$\rho_i C_p \frac{\partial}{\partial t} T_s = -k \frac{\partial}{\partial z} T + F_s - \sigma T_s^4 \tag{A3}$$

where F_s is the absorbed solar energy flux and σ is the blackbody constant.

The ice thickness $H = z_0 - z_b$ evolves due to melting and flow convergence as:

$$\frac{\partial}{\partial t} H = -\frac{1}{r} \frac{\partial}{\partial r} \left(r \int_{z_b}^{z_0} u dz \right) - M \tag{A4}$$

Our model assumes that any density change in a vertical column must be compensated by local vertical expansion/contraction — if we create melt somewhere, the volume loss from contraction on melting is compensated by a lowering of the ice surface z_0 above that point. It turns out that this is mathematically identical to an assertion of Archimedean isostatic balance for a floating ice sheet, with the "water line" at $z = 0$. We must ensure that at all times

$$z_b \approx z_{b\text{isostatic}} = -H \frac{\overline{\rho_i}}{\rho_w} \tag{A5}$$

where ρ_w is the density of water at the freezing point (assumed to be 1000 kg m^{-3}) and $\overline{\rho_i}$ is the mean density of the vertical ice column. In practice, we ensure that this is the case by relaxing z_b toward isostatic equilibrium on a timescale γ which is fast compared to other model dynamics:

$$\frac{\partial}{\partial t} z_b = -\frac{\overline{\rho_i}}{\rho_w} \frac{\partial}{\partial t} H - \gamma (z_b - z_{b\text{isostatic}}) \tag{A6}$$

Flow Velocity: To find the ice flow velocity u, we must first compute the pressure gradients within the ice. Hydrostatic balance tells us:

$$\frac{\partial}{\partial r}p = \frac{\partial}{\partial r}\left(\int_z^{z_0} g\rho_i(z')dz'\right) = \int_z^{z_0} g\frac{\partial}{\partial r}\rho_i(z')dz' + \rho_i(z_0)g\frac{\partial}{\partial r}z_0 \tag{A7}$$

We assume this pressure gradient force is balanced by a vertical gradient of horizontal shear stress (S_{rz}) within the ice:

$$\frac{\partial}{\partial z}S_{rz} = \frac{\partial}{\partial r}p \qquad \rightarrow \qquad S_{rz} = \int_{z_b}^{z}\frac{\partial}{\partial r}p \tag{A8}$$

where we assume the stress is zero at the base of the ice, which is valid when the ice is floating, but invalid when the ice is grounded. Though this would make the base of the grounded ice flow too fast, the pressure gradients are essentially zero for the grounded ice, so it makes little difference to the results of the model. We use the *Goldsby and Kohlstedt (2001)* flow law to find the strain rate $\dot{\epsilon}$ resulting from the horizontal shear stress, which is related to velocity as follows:

$$u = \int_z^{z_0}\dot{\epsilon} \tag{A9}$$

where we assume the ice is perfectly rigid (u=0) at the surface. In using the Goldsby flow law, we assume a grain size of 1 mm for most of our experiments, though using larger grain sizes does not change the result.

[Figure A1]

Model Grid: Figure A1 shows the geometry of the axisymmetric cylindrical model grid. Model discretization in r is fairly straightforward: u is modeled at r=0, dr ... L_r, and T is modeled at r=dr/2, 3dr/2, 5dr/2, ... L_r + dr/2; this choice makes it easy to satisfy the boundary condition requiring u = 0 at r = 0. Derivatives are represented using centered second-order finite difference schemes, except for the advection term, which requires an upwind first-order derivative for numerical stability.

For the vertical discretization, we define a new height variable s:

$$s = N_z\frac{z - z_b}{z_0 - z_b} \tag{A10}$$

so s = 0 at the base of the ice shell and $s = N_z$ at the surface. T and u are modeled at s = 1, 2, ... N_z. However, we must convert all derivatives from z to s:

$$\left.\frac{\partial}{\partial r}\right|_z = \left.\frac{\partial}{\partial r}\right|_s + \left.\frac{\partial s}{\partial z}\,\frac{\partial z}{\partial r}\right|_s\frac{\partial}{\partial s} \tag{A11}$$

$$\frac{\partial}{\partial z} = \frac{\partial s}{\partial z}\frac{\partial}{\partial s} = \frac{N_z}{z_0 - z_b}\frac{\partial}{\partial s} \tag{A12}$$

$$\left.\frac{\partial}{\partial t}\right|_z = \left.\frac{\partial}{\partial t}\right|_s + \left.\frac{\partial s}{\partial z}\,\frac{\partial z}{\partial t}\right|_s\frac{\partial}{\partial s} \tag{A13}$$

The second term in Equation A13 is particularly important: since the s-points are not stationary, they can move through vertical property gradients, which s-points see as an apparent change in the property over time.

Centered second-order finite differences are used for discretization in s, except for the "gridpoint motion" term just described, which requires an upwind first-order scheme for numerical stability.

The *s*-coordinate scheme allows us to resolve the thermal structure of the ice no matter how thin it gets, but there are two drawbacks. First, the increased mathematical complexity slows the computation somewhat. Second, as the ice becomes thinner and the vertical spacing between *s*-points decreases, the maximum permissible timestep decreases, becoming zero as the ice thickness goes to zero. If total melt-through to the surface actually occurred, a Zeno's paradox would result, and the model would never finish running. Fortunately, for our parameter choices to investigate heat flow on Enceladus, the analytical solution for equilibrium ice thickness never reaches zero, so the numerical solution does not approach this paradox.

Timestepping is performed using an explicit Runge-Kutta (2,3) method with an adaptive timestep (`ode23` in Mathworks' MATLAB™ 7).

Cylindrical versus spherical geometry: Our model uses cylindrical coordinates centered on the pole, and does not account for the spherical geometry of the real satellite. The cells in our cylindrical model will become increasingly too large with respect to a spherical model as one moves farther from the central axis. At 45° latitude from the center, this dimensional effect is about 10%, too small to have any significant effect on our model, especially considering that all the action is near the center. Only in a truly equator-to-pole model would this change in geometry become a problem.

The convergence of radii toward the center of the body also means that we overestimate the surface area of model cells deep within the satellite. However, since our deepest cells are only 25% of the way to the center, this factor is small compared to the uncertainty in the thermal power flowing through these cells, and is negligible at the shallow depth of the equilibrium ice base, which is the most sensitive part of the model for our results.

Table A1: Model Parameters

Variable	Description	Value
Nr	Number of radial gridpoints	100
Nz	Number of vertical gridpoints	20
Lr	Horizontal domain size, km	500
F_{solar}	Mean solar heat flux, W m^{-2}	1.2
ρ_{water}	Density of liquid, kg m^{-3}	1000
ρ_{ice}	Density of ice, kg m^{-3}	$-3.450 \times 10^{-4}\ T^2 + 3.411 \times 10^{-2}\ T + 934$ [a]
γ	Isostatic adjustment rate, yr^{-1}	1/20,000
C_p	Heat capacity of ice, J kg^{-1} K^{-1}	$7.037\ T + 185$ [b]
k	Thermal conductivity of ice, W m^{-1} K^{-1}	$488/T + 0.468$ [c]
L	Latent heat of fusion, J kg^{-1}	3.3×10^5
g	Surface gravity, m s^{-2}	0.114
$d_{goldsby}$	Grain size for Goldsby flow law, mm	1

Notes: [a] Eisenberg and Kauzmann, 1969; [b] Dorsey, 1940; [c] Hobbs, 1974.

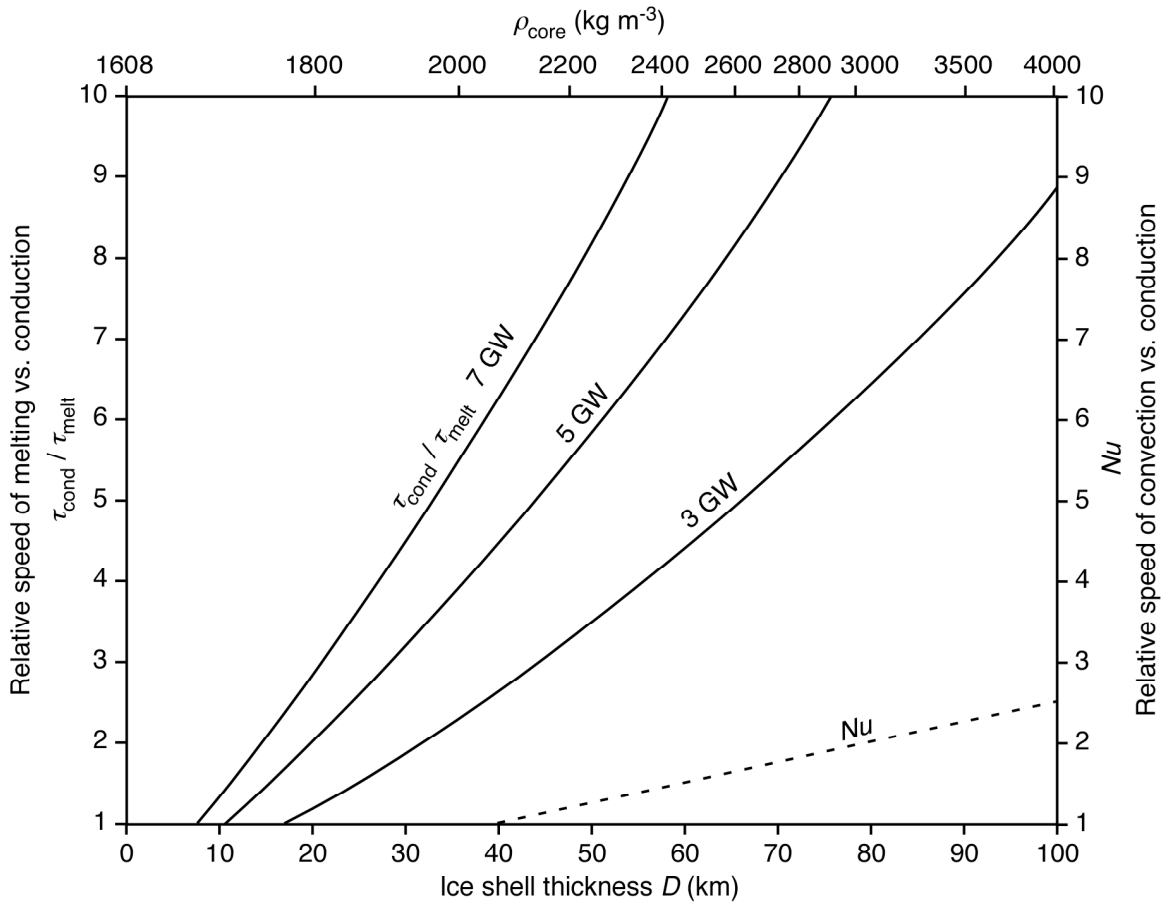

Figure 1. For ice thicker than 20 km, heating and melting the ice on Enceladus transports heat faster than conduction or convection. The top three curves show $\tau_{cond} / \tau_{melt}$ for basal heat fluxes of 3, 5, and 7 GW. A value of $\tau_{cond} / \tau_{melt} = 2$ means that heating and melting all of the ice of thickness D poleward of 50°S is twice as rapid as the characteristic conduction timescale $D^2 \kappa^{-1}$. The bottom curve shows the Nusselt number at thickness D, which shows the relative efficiency of convective heat transport to conduction.

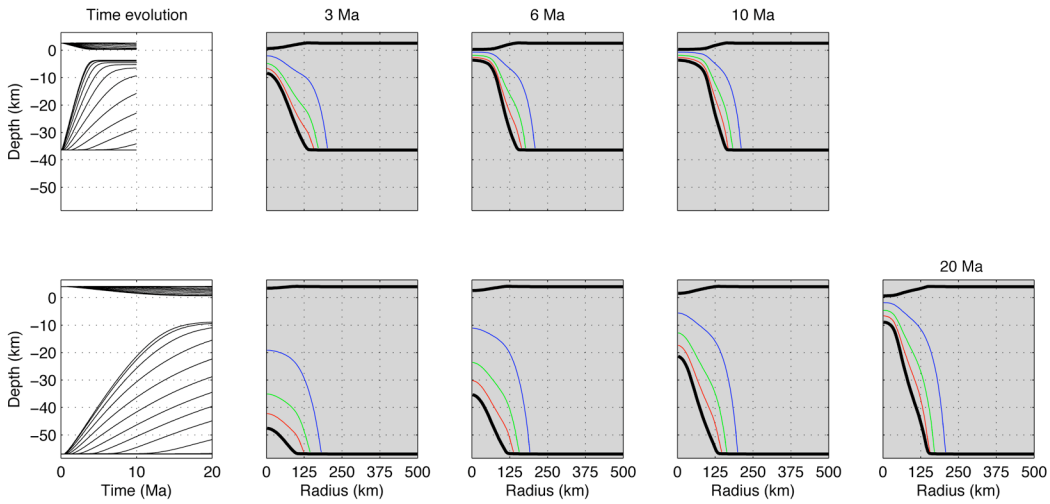

Figure 2. Response of a thermal conduction / ice flow model to basal heating of Enceladus's ice layer. First column: Time evolution of the position of the ice surface and base at several horizontal positions (plotted for every third gridpoint in the model). Columns 2-5: Shape of ice shell at several points in time. The thick dark lines indicate the positions of the top and bottom of the ice shell, and the thin colored lines indicate temperature contours within the solid ice (in order from bottom to top: 200 K - red, 150 K - green, and 100 K - blue). Most of the ductile ice flow occurs between the 200 K contour and the bottom of the ice. A Gaussian-bump heat source 300 km in diameter is applied beginning at t=0 to an ice shell initially in thermal equilibrium with a radiogenic-only rocky core. First row: 7 GW basal heat source, initial shell thickness 39 km. Second row: 3 GW heat source, initial thickness 61 km.

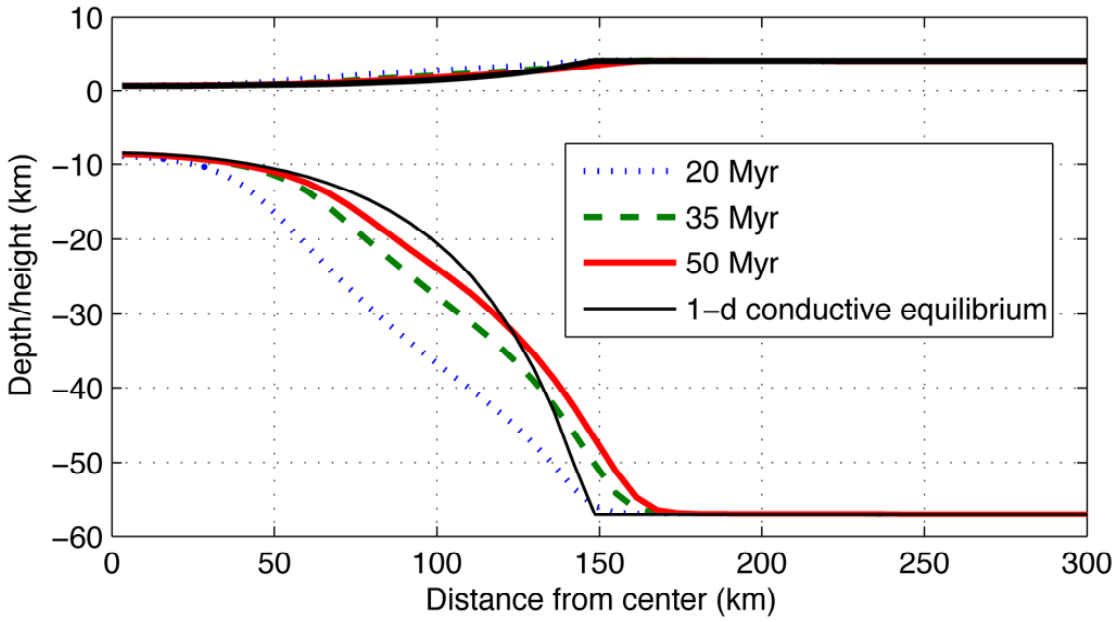

Figure 3. Evolution of the melting model over longer time scales than shown in Figure 2. The end of the model run on the bottom row of Figure 2 is shown as the 20 Myr line, and beyond this time the model slowly and asymptotically approaches an equilibrium close to the 1D conductive equilibrium line (calculated using equation 2), shown as a thin line on this graph. The deviation of the 50 Myr line from the conductive equilibrium line shows the effect of ice flow along the edge of the sea.

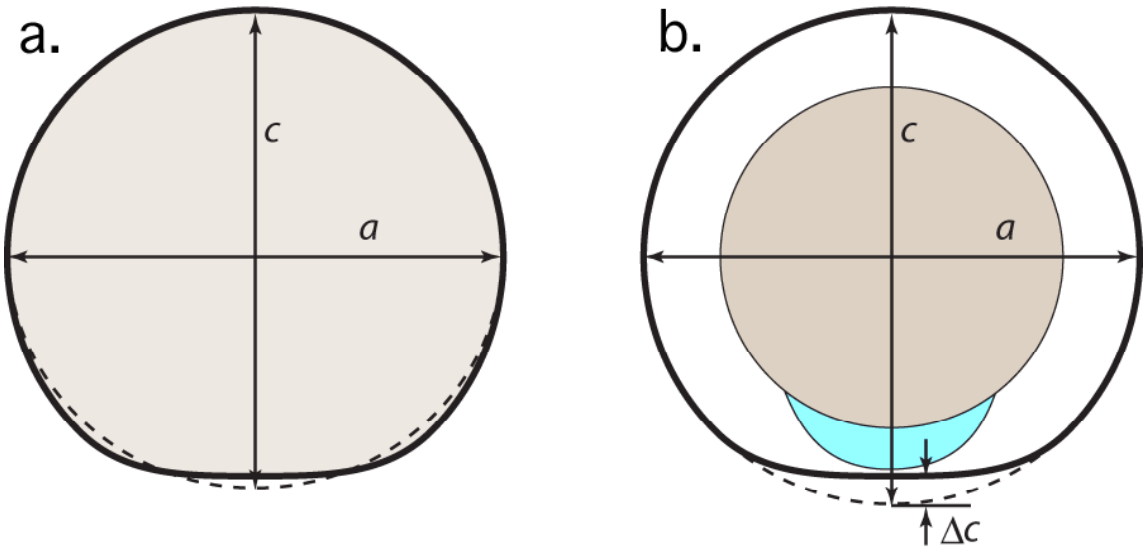

Figure 4. Internal structure models for Enceladus. a. The Porco *et al*. (2006) best fit to observed *a, b, c* axes is internally homogeneous. The largest reported deviations from the true shape of Enceladus lies below the best-fit ellipsoid at the pole, and above the ellipsoid at 50° S. b. Our best fit model is internally differentiated, and the modification of the *c* axis length (Δc) is explained by a large south polar depression created by basal heating and melting. The pit formed by melting flattens the south polar area, leading to the shape deviations observed by Porco *et al*.

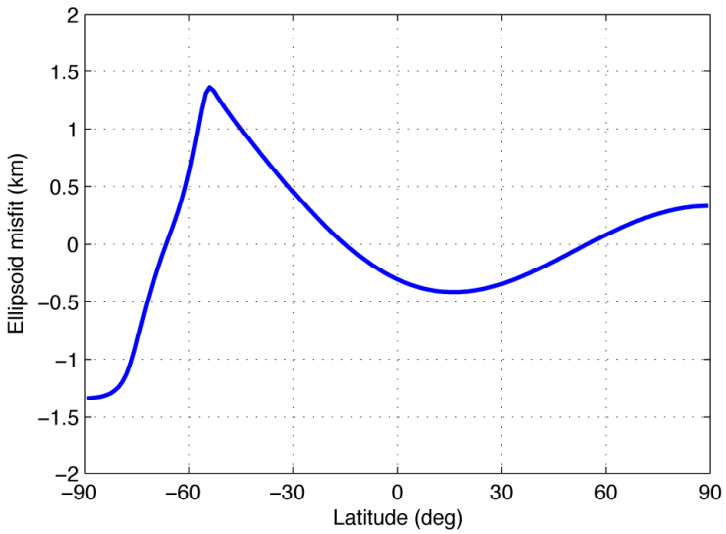

Figure 5. If we take an equilibrium ellipsoidal shape for a differentiated Enceladus (a=256.1, b=251.6, c=250.1) and melt a depression in the south polar zone as modeled in Figure 2 (lower row), the resulting global shape shows deviations from ellipticity larger than observed by Porco *et al*. (2006). The curve shows deviations from the reference ellipsoid (a=256.4, b=251.9, c=249.0) which best fits the post-melting shape. Note that the best-fit ellipsoid to the entire surface no longer has the same axial lengths as the original ellipsoid, and the residual topography shows a global low at the south pole, a global high at about 50°S latitude, as reported by Porco *et al*. (2006), while also producing smaller regional low just north of the equator and a regional high at the north pole, both of which appear in the global shape data (Thomas *et al*., *Icarus*, submitted).

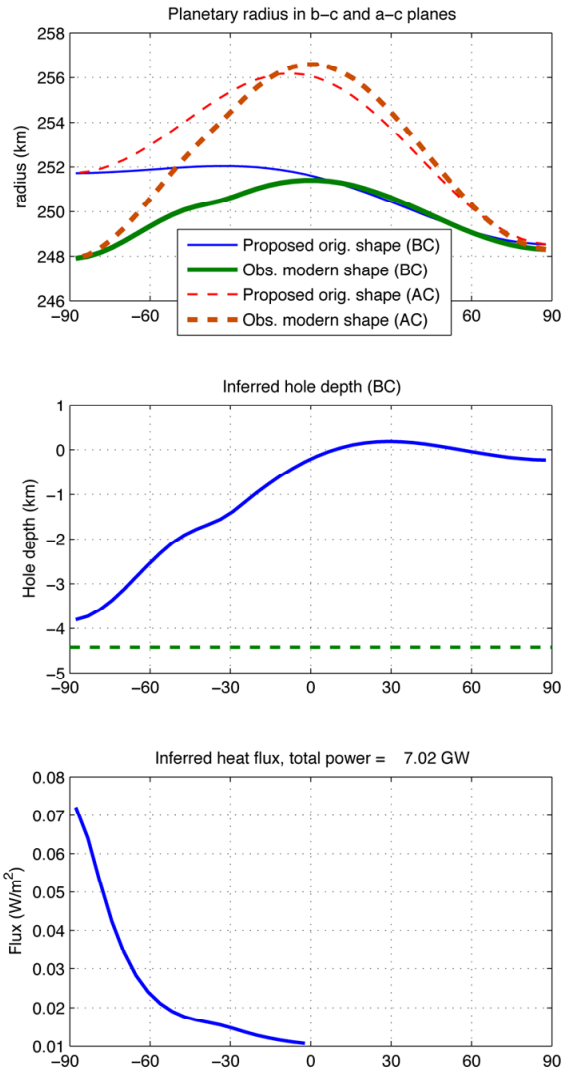

Figure 6. Inverse calculation to compute a melting profile which explains Enceladus's present shape. In this example, we assume a core density of 2600 kg m^{-3} and a starting mean radius of 252.6 km. Top: Planetary radius as a function of latitude for Enceladus as reported by Porco *et al*. (thick lines), compared to our proposed original pure ellipsoidal shape (thin lines). The asymmetry of the original shape curves occurs because the center of this ellipsoid has been shifted, allowing us to closely align the proposed and observed northern hemisphere shapes (step 3 in text). Middle: Surface depression required to account for difference in shape between observed shape and original ellipsoid. Bottom: Conductive heat flux required to melt sufficient ice to create the depression in the middle panel.

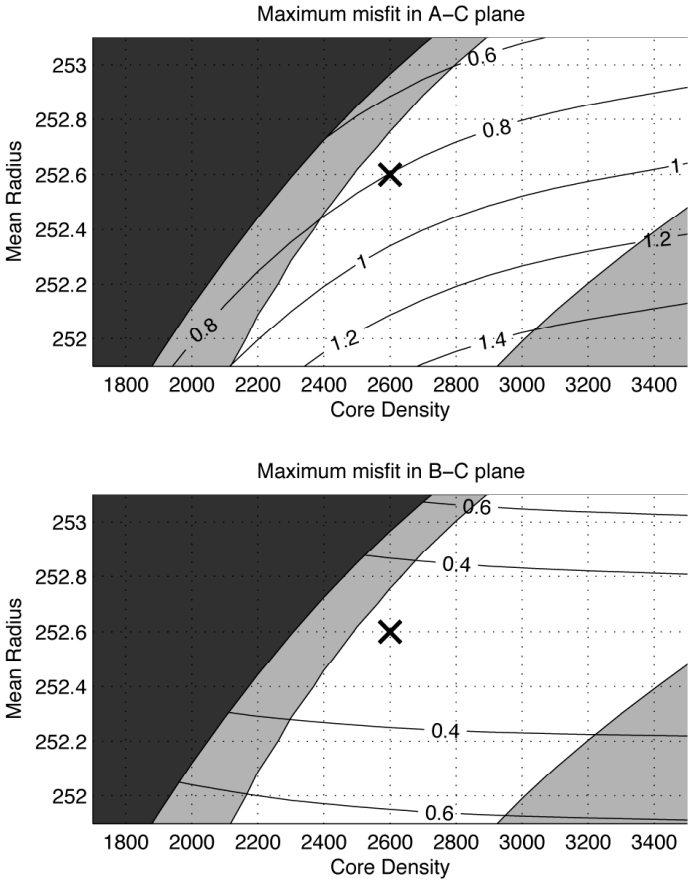

Figure 7. Parameter space exploration of mismatch between Enceladus's figure and the melted-ellipsoid model. X represents the choice of core density and mean radius used in Figure 6. Within the dark shaded area on the left, the planetary ice shell is too thin to produce a south polar pit of the required depth, even if the entire shell is melted. In the light shaded areas, the required basal heat source is more powerful (left) or less powerful (right) than observed. Top panel: Worst mismatch (always occurring in northern hemisphere) between reported shape of Enceladus and the shape of our proposed melted ellipsoid, in A-C plane (difference between dashed curves, top of Figure 6). Contours are in km. The 0.8 km misfit in this plane may be contained in the errors to the a axis fit, and the <400 m residual topography in the northern hemisphere not reported by Porco *et al*. (2006). Bottom panel: Same, for B-C plane (difference between solid curves, top of Figure 6).

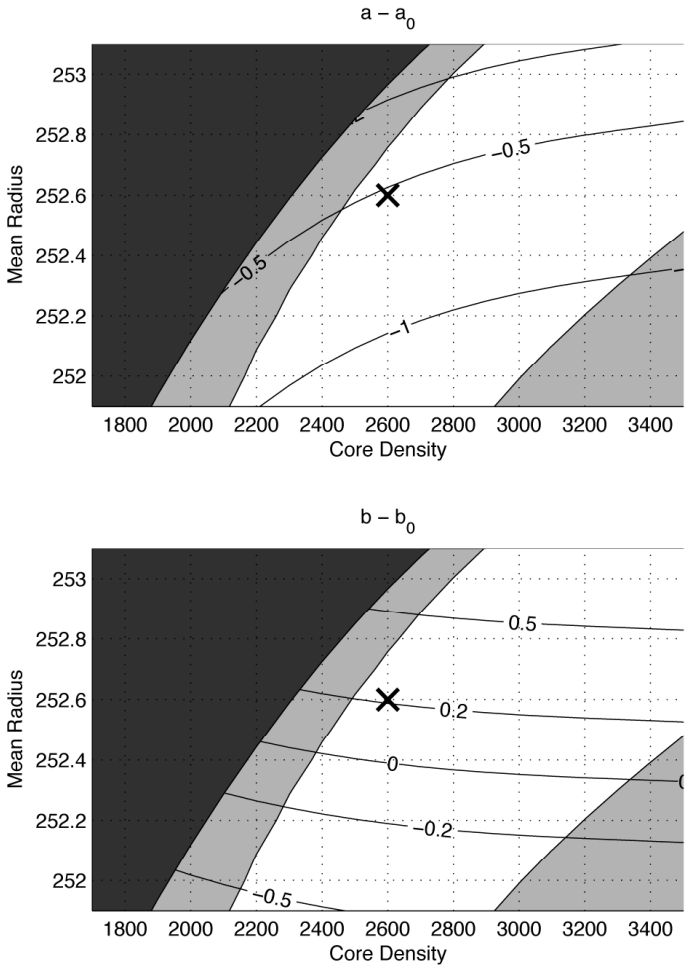

Figure 8. Mismatch (in km) between axis lengths of our proposed melted ellipsoids and the axis lengths reported by Porco *et al*. X indicates the parameters chosen for Figure 6. Shading is the same as Figure 7. Top: Difference in *a*-axis lengths. Bottom: Difference in *b*-axis lengths. The *c*-axes are nearly identical by the construction of the model. Note that error bars for *a* and *b* from Porco *et al*. are 0.5 and 0.2 km, respectively.

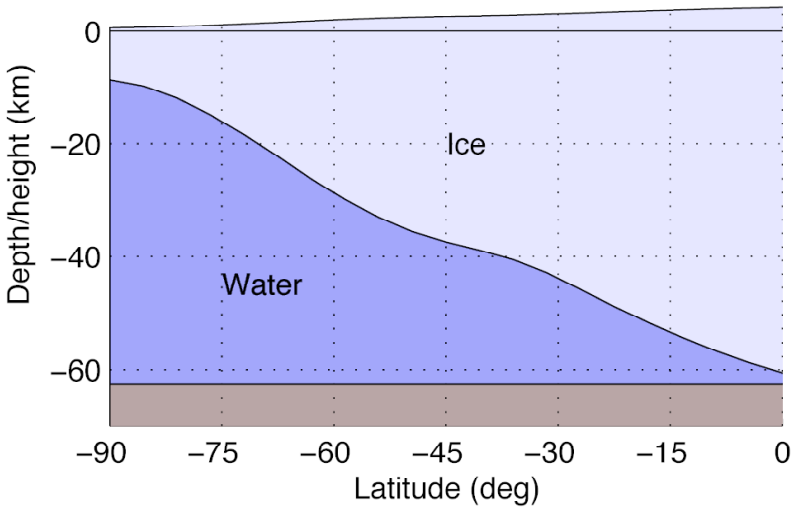

Figure 9: Geometry of sea from inverse model shown in Figure 6. The degree-2 gravity anomaly was calculated by the method used by Nimmo and Pappalardo (2006), but using stacked cylinders centered at the pole, with the edges of the cylinders approximating the ice-water boundary.

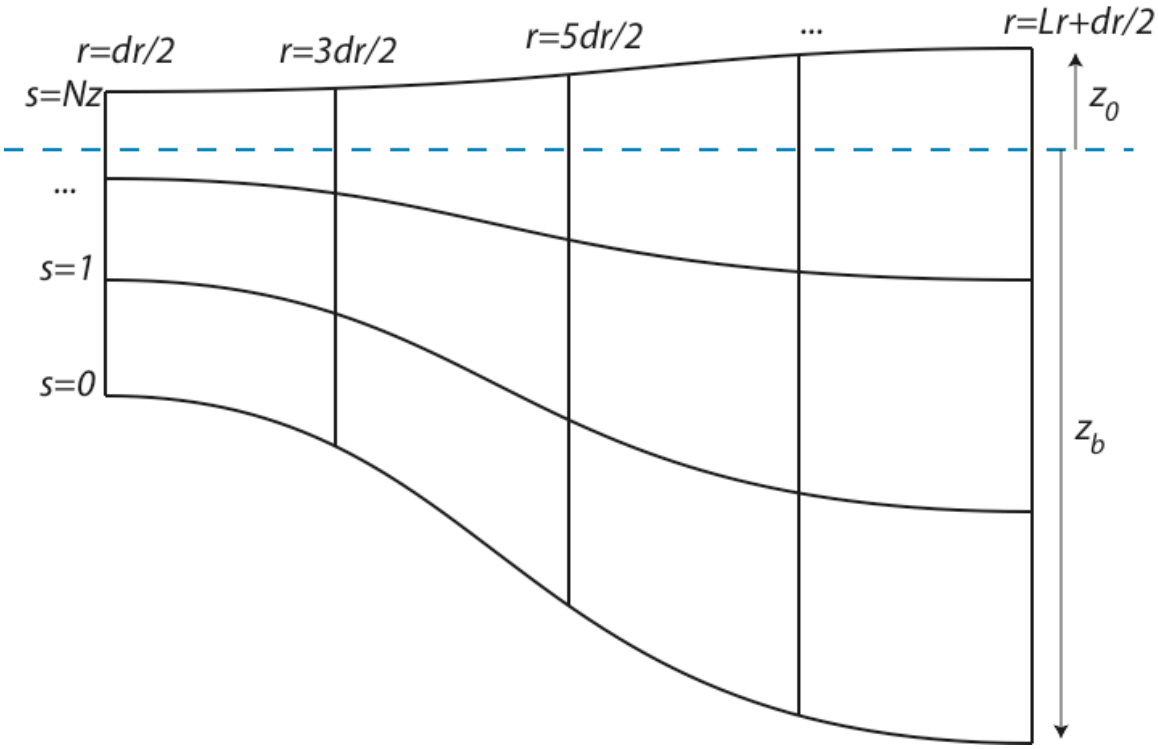

Figure A1: Model grid, showing definition of horizontal and vertical coordinates. Note variable vertical grid spacing.